Design of a Magnetic Gear for NASA's Vertical Lift Quadrotor Concept Vehicle

Thomas F. Tallerico[1] Zachary A. Cameron [1] and Dr. Justin J. Scheidler[1]
NASA Glenn Research Center, Cleveland, Ohio, 44135, U.S.A.

Magnetic gears are an attractive alternative to mechanical gears for electrified aircraft drive systems due to their ability to transmit torque without mechanical tooth contact. Consequently, magnetic gears enable electrified aircraft to take advantage of the benefits of gearing without introducing most of the contact-related reliability concerns associated with mechanical gearing. Magnetic gears however, have not been shown to match the specific torque (torque per unit mass) and efficiency of their mechanical counterparts in an aerospace application to date. In this paper, the design of a concentric magnetic gear for a NASA personal-air-transport reference vehicle is presented to demonstrate the feasibility of a magnetic gear for aerospace applications.

I. Nomenclature

B	=	magnetic flux density	T	=	period of magnetic flux repetition
l	=	magnet axial lamination size	w	=	magnet width
k_1	=	modified Stienmentz coefficient	V	=	magnet volume
GR	=	gear ratio	α	=	Stienmetz frequency coefficient
M	=	iron mass	β	=	Stienmetz Flux Density coefficient
Q	=	number of pole pieces	ρ	=	resistivity of magnet material
PR	=	number of ring gear pole pairs			
PS	=	number of sun gear pole pairs			
t	=	time			

II.   Introduction

Magnetic gears are an attractive alternative to mechanical gears in electrified aircraft applications, because of their ability to transmit torque without mechanical tooth contact between gear bodies. The use of a gearbox in the drive system of an electrified aircraft has been shown to significantly reduce overall drive system weight (Ref 1). However, the numerous failure mechanisms associated with mechanical tooth contact in traditional gearing results in a significant reliability penalty (Ref 2-3). Magnetic gears' ability to transmit torque without mechanical tooth contact eliminates these failure mechanisms, reducing maintenance costs and increasing reliability. To date, most of the development of magnetic gears has been focused toward wind energy, marine energy, and automotive applications where volumetric torque density (torque per unit volume) has been the primary objective (Ref 4-8). In contrast, electrified aircraft drives' primary design objectives are specific torque (torque per unit mass) and efficiency (Ref 9-10).

In 2016, NASA launched a program to develop magnetic gears for electrified aircraft applications (Ref 11-14). As part of this program, NASA has produced three prototype magnetic gears. The first (PT-1) was used as a proof of concept gear made of commercial-off-the-shelf parts (Ref 11). The second (PT-2) was designed to demonstrate the feasibility of making a magnetic gear as light weight as its mechanical counterpart (Ref 11-14). It currently is the highest specific torque magnetic gear prototype reported in the open literature. The third prototype (PT-3) was a high efficiency version of PT-2 meant to demonstrate the feasibility of magnetic gears to have efficiency similar to their mechanical counterparts.

This paper presents the design of NASA's fourth prototype concentric magnetic gear (PT-4). It is meant to demonstrate the feasibility of producing a magnetic gear that is both as efficient and light weight as its mechanical counterparts. It also is the first known magnetic gear to be designed using a combined electromagnetic and structural design code. PT-4 is designed specifically for NASA's personal air transport reference vehicle designed within NASA's Revolutionary Vertical Lift Technology (RVLT) project (Ref 15). The RVLT quadrotor reference vehicle, shown in Figure 1, is a single passenger, autonomous, all electric "air taxi" aircraft. It has four rotors that each spin at

---

[1] Aerospace Research Engineer, Rotating and Drives Systems Branch.

680 RPM and require a shaft torque of 226 Nm. The required shaft power is 16.1 kW. In the initial aircraft concept design, each of these rotors is driven by a geared electric motor that spins at 8000 RPM. The gearboxes for this motor and rotor combination therefore have a gear ratio of roughly 12 to 1 (Ref 11). For PT-4, mass and efficiency targets where set at 4.5 kg (~50 Nm/kg) and greater than 97% efficiency respectively. Based on the promising specific torque results of NASA's first three prototypes (Ref 11-14), the chosen magnetic gear configuration for PT-4 is a concentric magnetic gear.

In section three of this paper, a brief description of concentric magnetic gears will be provided. Section four will discuss the design code developed to produce PT-4's preliminary design. Section five will discuss the final magnetic design and the projected efficiency of the gear. Section six will discuss the thermal design of the gear. Finally, section seven will discuss the structural design of the gear and the deviation of the final design from the design code results.

Figure 1 NASA's RVLT Quadrotor Air Taxi Reference Vehicle
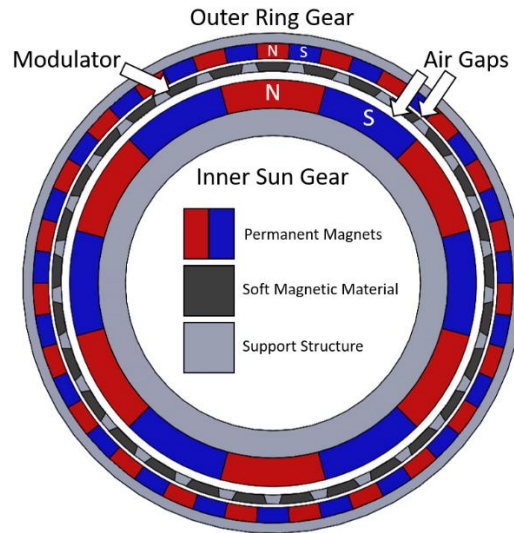
III.   Concentric Magnetic Gears

Figure 2 Cross-section of a simple concentric magnetic gear

The concentric magnetic gear (CMG), shown in Figure 2, was first proposed in 2003 (Ref 16). Since then, it has been extensively studied because of its high volumetric torque density. A CMG consists of three concentric rotors: a sun gear, a ring gear, and a modulator. The sun gear is a low pole count permanent magnet rotor that is typically used as the high-speed input to the CMG. The ring gear is a high pole count permanent magnet rotor. The modulator is a rotor that consists of alternating sections of high magnetic permeability material (pole pieces) and low magnetic permeability material (air, plastic, carbon fiber, etc.). The modulator sits in-between the sun and the ring gear and spatially modulates both permanent magnet rotor's magnetic fields so that they have the same spatial harmonic order

in both airgaps. With matching spatial harmonic order in both airgaps, the magnetic fields are able to couple and transmit torque continuously between all three rotors. In order to modulate the fields optimally, the number of pole pieces in the modulator is selected such that

$$Q = PR \pm PS \qquad (1)$$

Where Q is the number of evenly spaced pole pieces in the modulator, PR is the number of ring gear pole pairs, and PS is the number of sun gear pole pairs. For a detailed explanation of how the modulator couples the sun and ring gear together, the reader is referred to references 11 and 12.

Either the ring gear or the modulator can be held stationary while the other one rotates. If the modulator is held fixed, the CMG's gear ratio is given by

$$GR = \frac{PR}{PS} \qquad (2)$$

If the ring gear is held fixed, the gear ratio is given by

$$GR = \frac{Q}{PS} = \frac{PR}{PS} \pm 1 \qquad (3)$$

A higher overall gear ratio with the same sun and ring gear pole counts can be achieved by selecting the number of pole pieces in the modulator to be the sum of the ring and sun pole pair counts, and holding the ring gear fixed, while using the modulator as the gear's output. This configuration of the CMG was therefore selected for study by NASA, and is used for PT-4.

IV. PT-4 Magnetic Gear Design Code

Axial segmented magnets with electrically insulating epoxy between each segment, called magnet laminations in this paper, are often used in permanent magnet motor design to reduce rotor magnet eddy current loss. NASA's third magnetic gear prototype, PT-3, demonstrated that >98% efficiency is achievable in a CMG if the sun and ring gear magnets are laminated sufficiently. Additionally, preliminary studies on the potential efficiency of a magnetic gear for the quadrotor concept vehicle showed that axial magnet laminations of less than 2 mm would allow the design to achieve higher than the targeted 97% efficiency. Section 5 of this paper discusses the effect of magnet lamination size on PT-4's efficiency to illustrate this point.

The bulk of the design work for PT-4 was therefore focused on achieving the 4.5 kg mass target. A combined electromagnetic and structural magnetic gear design code was developed to study the design space and create the PT-4 preliminary design. A combined structural and electromagnetic design code had to be used in the preliminary design process, because of the high coupling of the electromagnetic and mechanical design consideration in a CMG. In particular, pole piece radial thickness and the size of the sun-to-modulator magnetic air gap are two highly influential design variables in the electromagnetics of a magnetic gear. Both dimensions are limited by structural considerations. Additionally, the size and radial location of the magnetic components contribute significantly to bearing loading and the mass of the structure needed to support the magnetic components.

The architecture of the developed magnetic gear design code used for PT-4 is depicted in Figure 3. The code requires initial values for radius, gear ratio, output torque, sun gear pole pair count, and input speed. It then runs cases of the thicknesses of the electromagnetic component (sun gear magnets, pole pieces, and ring gear magnets) through the electromagnetic and structural analysis modules of the code to create a total gear mass estimate. A minimum search algorithm then uses these mass estimates to iterate the three magnetic component thicknesses and optimize the mass of the gear. The different modules of the code will be discussed in the next 2 sections of this paper. A discussion of the codes results used for PT-4 follows.
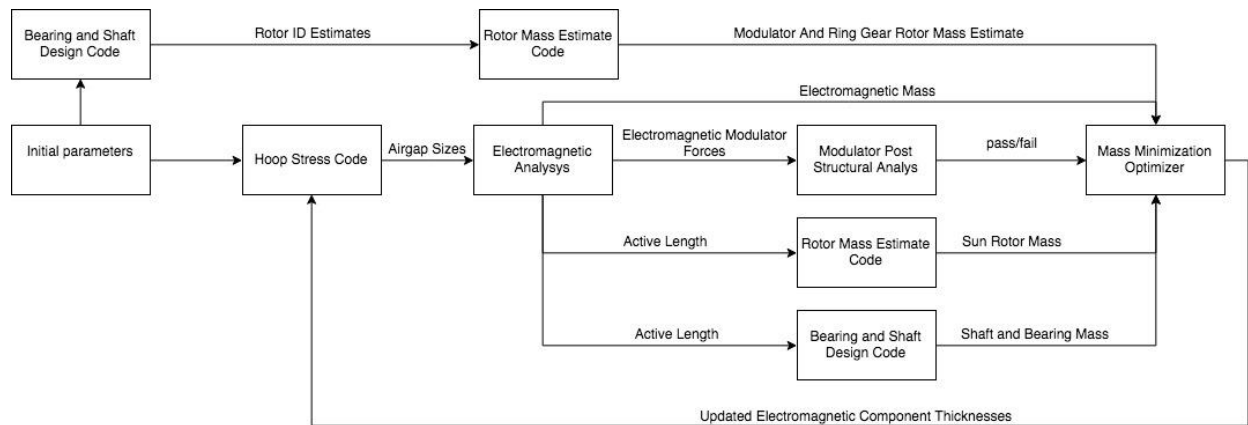
Figure 3 Magnetic gear design code flow diagram

A. Mechanical Components of the Design Code
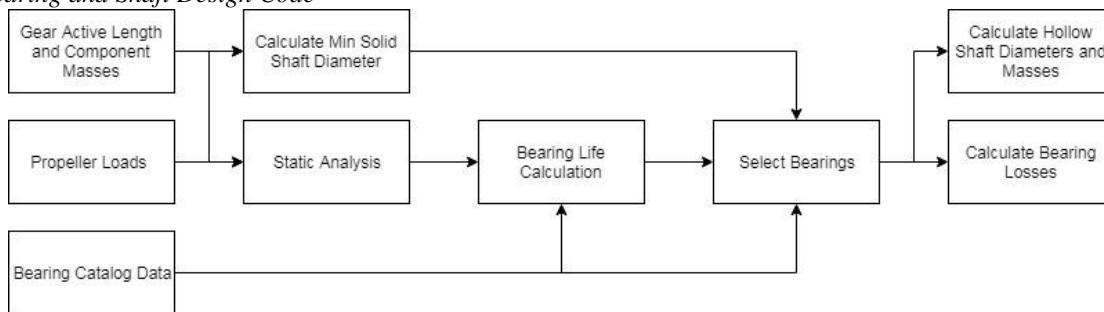### 1. *Bearing and Shaft Design Code*

Figure 4 Bearing and shaft design code flow diagram

A flow diagram for the bearing and shaft design code is shown in Figure 4. In PT-4's design, estimates of the aerodynamic, gyroscopic, thrust, and torque loads for the RVLT quadrotor were accounted for in the bearing and shaft designs. The estimates of those loads, along with the assumed required life are listed in table 1.

Table 1 Estimated bearing loads and requirements in the design code

Load	Value
Required Bearing Life (99% Reliability)	10,000 Hours
Output Torque	226 Nm
Input Torque	18.8 Nm
Thrust Load	1400 N
Propeller Mass	10.5 Kg
Propeller Hub Moment (Worst Case)	1203 Nm
Propeller Hub Moment (Nominal Case)	604 Nm
Nominal Propeller Hub Drag	100 N
Max Turning Acceleration	2 G's
Nominal Yaw Rate	0.25 rad/s
Nominal Pitch Rate	0.25 rad/s

The layout of bearings and shafts for PT-4 is depicted in Figure 5. It was assumed that four bearings are used in the magnetic gear. Bearing one is assumed to be a double row bearing to counteract the moments and thrust from the propeller and avoid passing those loads through the modulator structure. The second bearing is also double row to minimize misalignment of the input and output shafts by increasing the area of contact between the two shafts. This minimization of misalignment is driven by a tight test rig shaft misalignment tolerance and may not be necessary in an actual gear box design. Bearing 3 is assumed to be a single row deep grooved ball bearing and bearing 4 is assumed

to be an angular contact bearing. Both shafts are assumed to be made out of steel with a max allowable stress of 300 MPa.
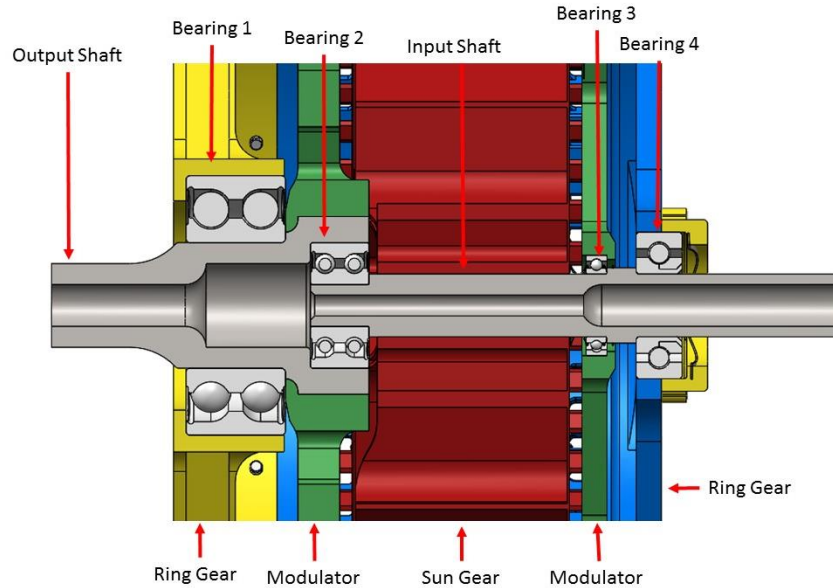

Figure 5 Cross-sectional view of PT-4 showing bearing and shaft layout

In each iteration of the design code, the bearing code takes in the current design's axial length, rotor masses, and radius. In the bearing code, the min required shaft thicknesses for both the input (sun gear) and the output (modulator) shafts are calculated. A static structural analysis is then used to calculate the peak and nominal loads on the four bearings. The peak loads are checked against the static load ratings of a set of bearings in a bearing database created from a manufacturer's catalog (Ref 17). Fatigue lives at the nominal loading are also calculated for every bearing in the database. Bearings whose bore diameter is not greater than the minimum shaft diameter, do not have static load ratings greater than the bearing peak loads, or do not have the required fatigue life are disqualified. The set of four bearings that minimize bearing mass are then selected from the remainder. Using the bore diameters of the selected bearings as the outer diameter of the sun and modulator shafts, the max inner diameters of both shafts are then calculated. Using the nominal loading and bearing efficiency equations from Reference 17, the frictional power loss in each of the four bearings is calculated. The bearing code then outputs a mass and power loss estimate for the bearings and the shaft sizes to the system-level design code.

2. Rotor Mass Estimation Code

Two-dimensional finite element analysis of a representative rotor section (Figure 6) was used to estimate the mechanical mass of the sun rotor, modulator end caps, and ring gear end caps. The ring and modulator end caps are defined in this paper as the axial end sections of both rotors that span the radial distance from the rotors' magnetic components to the gear's shafts and bearings. For the analysis of the ring and modulator rotors' axial caps, outer radii were set to the rotor outer radius and then the rotor rim thickness, rotor spoke thickness, and fillet radius were optimized to minimize the rotor mass at an axial length of less than 10 mm. The 10 mm limit was used to avoid optimum rotor cap designs that had unreasonable axial lengths. The sun rotor was optimized in a similar manner once the axial length of the active section of the gear was determined by the electromagnetic analysis. Mass estimates for the rotor structures were created with each design code iteration of the three magnetic component thicknesses to include in the code's estimate of total gear mass.
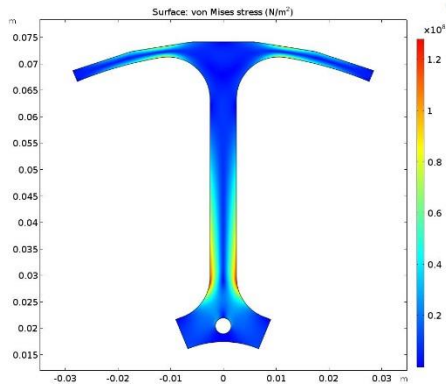
Figure 6 Example 2D rotor structural FEA

3. Hoop Stress Code

In order to set the magnetic airgap between the sun gear and the modulator, an iterative solver was used to estimate the required carbon fiber hoop thickness needed to contain the sun magnets for each design code iteration. The carbon fiber plies in the hoop were assumed to have a max allowable tensile stress of 600 MPa in the tangential direction. Centripetal loading of the hoop was calculated using the mass and rotational speed of the sun magnet. A non-linear analytical equation was used to calculate hoop stress. An initial hoop thickness was assumed equal to the thickness of two carbon fiber plies (0.25 mm). Hoop stress was calculated and the initial thickness was iteratively increased by the thickness of one carbon ply until the hoop stress was below the assumed max allowable tensile stress. The resulting hoop thickness was added to the assumed mechanical airgap to set the sun-to-modulator magnetic airgap in the electromagnetic simulations.

4. Modulator Post Structural Analysis

It was assumed that the modulator structure for PT-4 would be identical to the modulator structure used for PT-3. PT-3's modulator is depicted in Figure 7. It uses unidirectional carbon fiber posts between each of its pole pieces to transmit the load on each pole piece to the two end caps of the modulator. The stress in these posts typically limits the thickness of the pole pieces for a given axial length. The magnetically-optimum pole piece thickness is typically less than the mechanical limit. To account for this in the design code, with each iteration of the design the stress in the support posts was estimated. Electromagnetic forces were calculated for each pole piece in the electromagnetic simulations. The maximum of these forces was added to the centripetal forces on the pole pieces at operating speed. Euler-Bernoulli beam bending equations were then used to estimate the stress in the support posts assuming a trapezoidal cross-section, fixed-fixed boundary conditions, and a uniform distributed load. A stress limit for the posts of 800 MPa was set and designs that exceeded this limit were eliminated from consideration in the code's mass optimization.
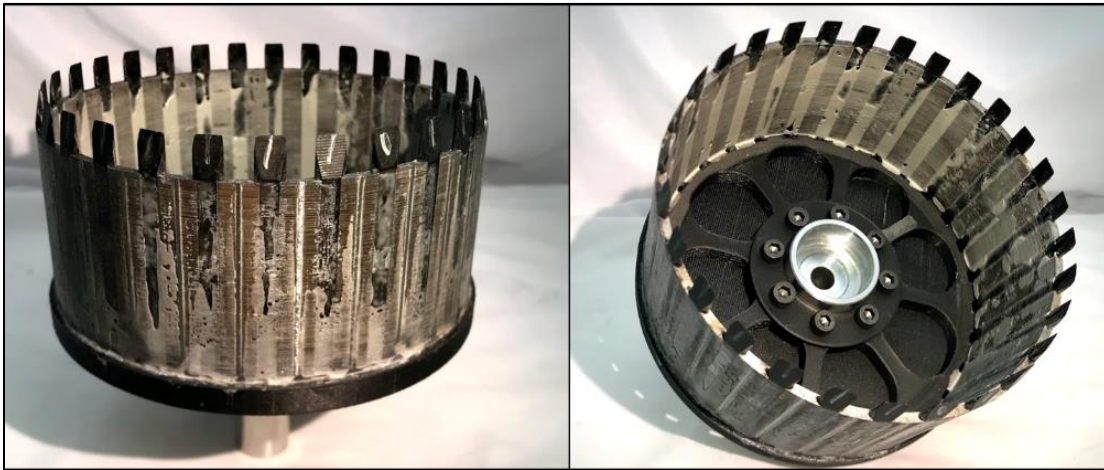

Figure 7 NASA's third prototype magnetic gear (PT-3) modulator (second end cap not shown).

6

B. Electromagnetic Analysis

The electromagnetics were simulated using a parameterized magnetic gear model in a commercial multiphysics finite element analysis (FEA) package. An example of the geometry used in the FEA simulations and the resulting magnetic field distribution for that geometry is shown in Figure 8. In this model, an integer gear ratio of 12:1 was used to make the ring magnets symmetric across a single sun pole arc. Using this symmetry, only an arc segment of the gear spanning one full sun pole pair was simulated, reducing computational cost. Integer gear ratios do however lead to large amounts of torque ripple and cogging torque in magnetic gears (Ref 19 and 20). The final gear design therefore should be updated from the design code results to have a non-integer gear ratio as is done in Section IV.
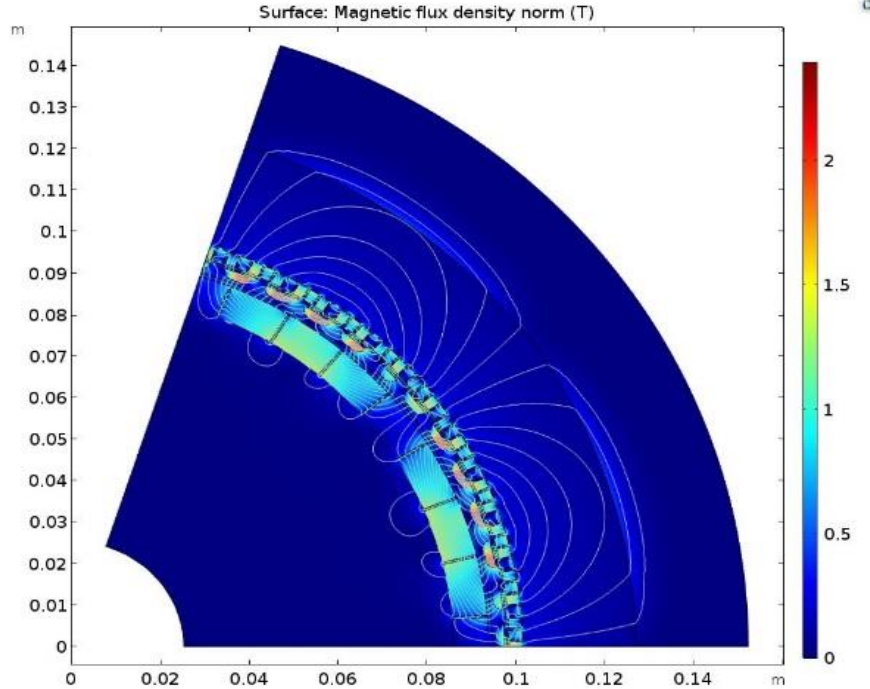

Figure 8 Example electromagnetic analysis used in the design code.

Both the sun and the ring gear magnetic arrays were Halbach arrays. The sun was assumed to have eight magnets per pole pair in its Halbach arrays, and the ring was assumed to have four magnets per pole pair in in its Halbach arrays. Each magnet was assumed to have a 0.5 mm thick non-magnetic wall between it and its neighbors for assembly considerations and to avoid dependence on glue bonds for torque transmission from the magnets to the structural components. A non-linear magnet model was used based on magnet B-H curves at the anticipated operating temperature.

The modulator pole piece geometry was created through the use of three pole piece span angles: outer, min, and inner. The definition of these span angles is shown in Figure 9. The three span angles were held fixed in the design code at values that had been determined by previous parametric simulations. Outer span angle and mid-span angle were both set to be equal to 120% of the ring gears' pole to pole distance. The inner pole piece span angle was set to be half that value. An example of this pole piece geometry used in these simulations is shown in Figure 8. The geometry used in the code is not the same as the final designs pole piece geometry, because the code's pole piece geometry does not enable a mechanical interlock between the pole pieces and their neighboring carbon fiber support posts. Nevertheless, the simplified geometry was used in the design code, because it was found to scale well with different input variables (Radius, Gear Ratio, etc.) and give reasonable estimates of the maximum achievable specific torque. As is described in Section V, the pole piece geometry is re-designed after preliminary design is complete to enable the mechanical interlock with the support posts.
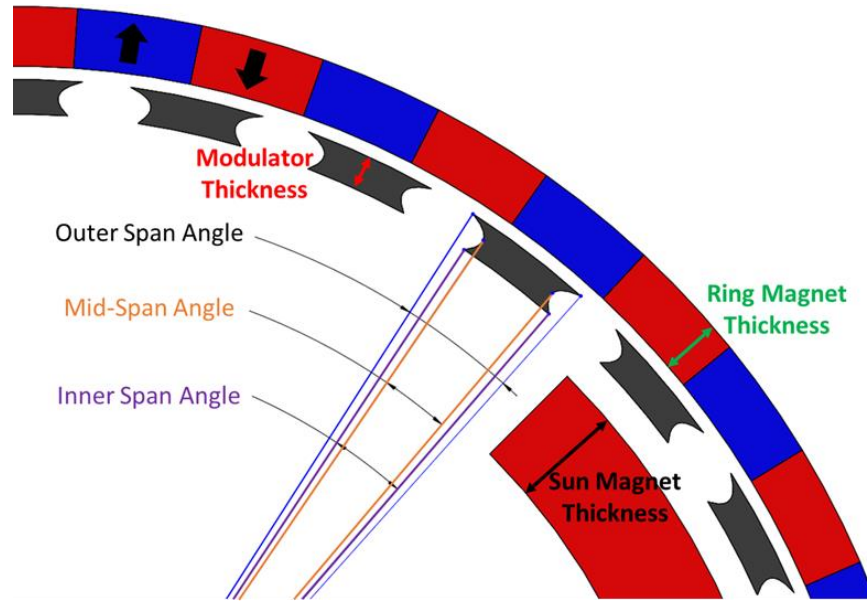
Figure 9 Pole piece span angle and component thickness definitions used in the design code. Some sun gear magnets are hidden and a simplified array are used for clarity.

Two-dimensional electromagnetic analysis always overpredicts the output torque of a CMG, because three-dimensional axial flux leakage effects are neglected (Ref 18). Axial leakage was accounted for in the code based on the aspect ratio of the gear (active axial length divided by diameter) using the leakage-effect estimates presented by Gerber in Reference 18. This estimation of axial leakage may not accurately predict PT-4's output torque. However, it is the only available correlation in the open literature for magnetic gear 3D leakage effects, and the use of 3D FEA simulations was determined to be too computationally expensive for the design code.
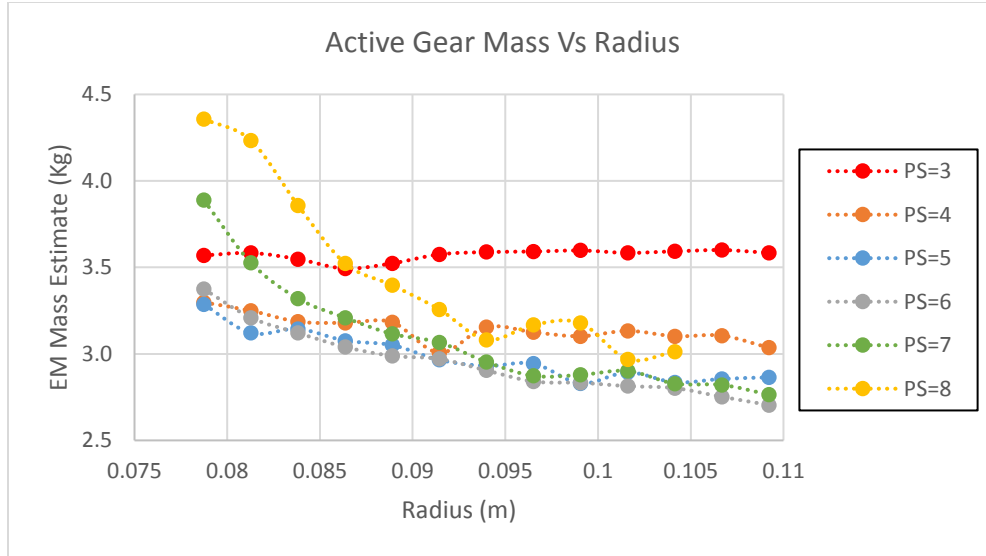
C. Design Code Results

In preliminary executions of the design code for an operating temperature of 100℃, gear designs using NdFeB magnet grades N48SH and N50H in their ring and sun gears were found to be incapable of meeting the mass target for the gear (4.5 kg). The targeted operating temperature was therefore lowered to 80℃. NdFeB grade N52M magnets are the highest grade NdFeB that has a specified operating temperature greater than 80℃. Thus, it was assumed that grade N52M would produce the highest specific torque gear at a gear operating temperature of 80℃ and the design code was only run for N52M at 80℃. This assumption was incorrect, as is shown in table 2, discussed in Section V, because N52M is significantly more susceptible to demagnetization at 80℃ than grade N50H and N48SH. However, PT-4's preliminary design was selected based on the results of the design code sweeps for N52M at 80℃. The total, mechanical, and magnetic mass results from the design code as a function of gear outer radius and sun gear pole pair count for grade N52M magnets at 80℃ are shown in Figure 10.
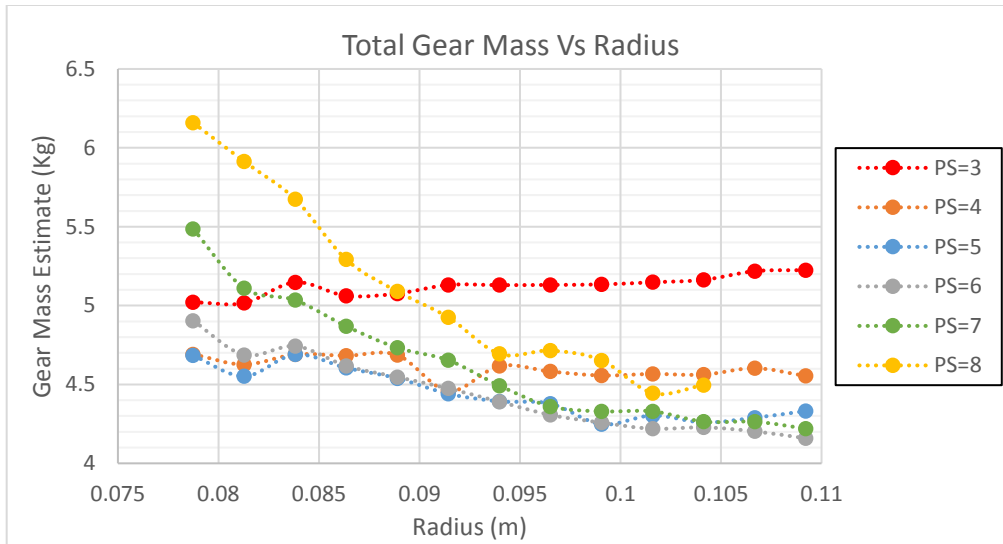
a) Total Gear Mass Results from the Design Code Parametric Sweeps of Radius and Sun Gear Pole Pair Count
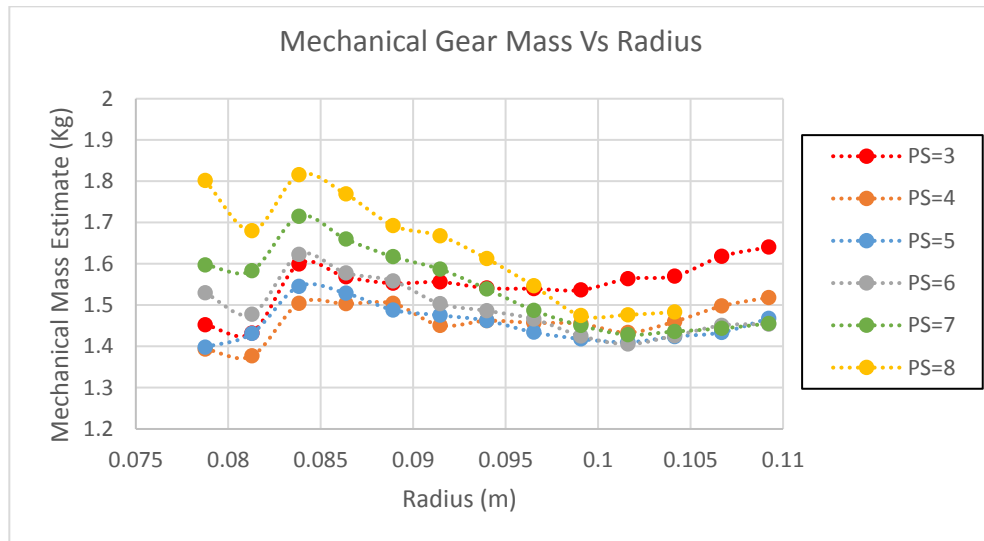
b) Gear Mechanical Mass Results from the Design Code Parametric Sweeps of Radius and Sun Gear Pole Pair Count

Active Gear Mass Vs Radius

c) Gear Magnetic Mass Results from the Design Code Parametric Sweeps of Radius and Sun Gear Pole Pair Count

Figure 10 Design code results for preliminary design of PT-4

The results in Figure 10a show that a gear with five, six, and seven sun gear pole pairs and a radius greater than approximately 92.5 mm is capable of achieving the mass requirement for PT-4. Smaller radii do not achieve the required mass because the magnetic components are put at less of a mechanical advantage. Sun gear pole pair counts less than five have higher mass, because, at the radii studied, they have larger pole-to-pole distances. Larger pole-to-pole distances both lower the specific flux of the magnetic arrays and requires additional pole piece thickness to create effective flux modulation.

High sun gear pole pair counts (seven or eight), at the radii studied, have higher masses, because of ring gear pole to pole magnetic flux leakage. Ring gear pole-to-pole leakage flux is flux that couples between ring gear poles through the ring gear-modulator airgap rather than coupling to the sun gear's flux through the modulator and producing torque. The percent of a ring gears' flux that leaks pole-to-pole is governed by the radial size of the ring gear-modulator airgap and the pole-to-pole distance on the ring gear. As the pole-to-pole distance on the ring gear gets smaller and becomes closer in size to the airgap, more and more flux leaks pole-to-pole because the reluctance of the pole-to-pole path becomes similar to the reluctance of the path across the airgap. Per Equation 3, gear ratio and sun gear pole pair count determine the ring gear pole pair count and therefore controls the ring gear pole-to-pole distance at a given radius. For a sun gear pole pair count of eight, at all radii studied, and for a sun gear pole pair count of seven at the smaller radii studied, ring gear leakage results in less torque being produced per unit axial length of the gear, and therefore a required longer axial length as compared to lower-pole-count gear designs. A steeper mass reduction with radius increase is seen for sun gear pole counts of seven and eight than for lower pole counts in Figures 10A and 10C. This steeper mass reduction with radius increase results from increased radius increasing the pole-to-pole distance on the ring gear and correspondingly reducing the ring gear pole-to-pole leakage flux that is significant in the higher sun gear pole count designs.

Mechanical mass has a significant step increase at a radius of about 83 mm in Figure 10b because of a required step change in the bearing selection resulting from higher gyroscopic bearing loads and a shorter axial length available to react moments. Except for that step change, there is a small, downward trend in mechanical mass in Figure 10b until a radius of 100mm resulting from reduced axial length with increased radius. Beyond the 100 mm radius size, mechanical mass grows due to the increased distance from the magnetic components to the shafts.

Based on the preliminary design code results, a 104 mm outer radius gear with five sun gear pole pairs was selected for PT-4. A sun gear pole pair count of five was selected because it was the lowest pole count to achieve the mass target. The 104 mm radius was selected because it was near the minimum for the five pole pair designs and had reasonable modulator and ring magnet thicknesses. To reduce torque ripple, the pole pair count of the ring was increased to 56 pole pairs from 55 and the modulator pole piece count was increased to 61 from 60 to create a non-integer gear ratio (Ref 19-20). Static electromagnetic, efficiency, thermal, and structural analysis was then performed to finalize the design.

V. PT-4 Electromagnetic Design and Efficiency

A. Static Electromagnetic Analysis

Static electromagnetic analysis was carried out on the selected design with the updated pole piece and ring gear pole pair counts in order to redesign the pole piece span angles. This re-design was done to enable a mechanical interlock between the pole pieces and the carbon fiber modulator support posts. Fillets were added to the corners of the pole pieces to eliminate sharp corners for manufacturing considerations. 2D FEA simulations of the selected design were run for parametric sweeps of the three pole piece span angles, shown in Figure 9, and a design was selected that maximized 2D specific torque. Figure 11 shows the final pole piece geometry.
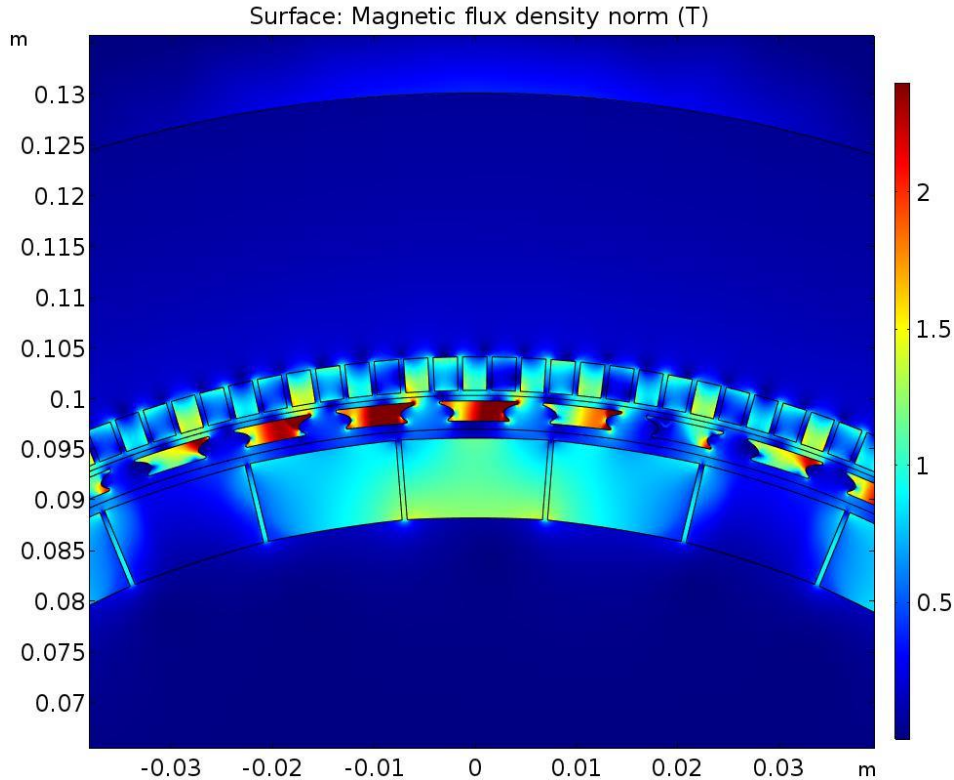

Figure 11 Electromagnetic simulation of final PT-4 design showing final pole piece geometry

Once the pole pieces were redesigned, demagnetization of the magnets was checked at an assumed 80℃ operating temperature. Figure 12 shows a plot of the magnetization magnitude in the magnets assuming N52M NdFeB ring magnets. A significant amount of demagnetization can be seen in the tangentially orientated magnets of the ring gear's magnetic Halbach arrays. In the design code, minimum ring magnet radial thickness of 3 mm had been held to avoid demagnetization of the ring gears radial magnets. However, with the high pole and magnet count of the ring gear, the width of each magnet was below this minimum value. Thereby, the length scale of the tangential magnets in their magnetization direction was less than 3 mm and significant demagnetization was possible. In order to correct for this, rather than re-optimize the gear, alternative grades of NdFeB that had higher maximum operating temperatures were substituted in for both the ring gear and the sun gear. Figure 13 show the resulting magnetization values for grade 48SH NdFeB ring magnets with N52M sun magnets. Compared to Figure 12 no significant ring gear demagnetization is noted. Table 2 shows the resulting torque values for various changes of ring and sun gear magnetic material. The table shows that an error was made in assuming that the highest-grade magnet with a specified operating temperature greater than the assumed maximum temperature would produce the highest specific torque magnetic gear. Due to the magnetic environment of a magnetic gear, magnets are much more likely to demagnetize than they would be in a synchronous permanent magnet machine where the demagnetizing field comes from a typically weaker electromagnet rather than a second set of permanent magnets.

For the final magnetic design grade N52M sun magnets and N48SH ring magnets were selected. Table 3 lists the magnetic design parameters for PT-4.
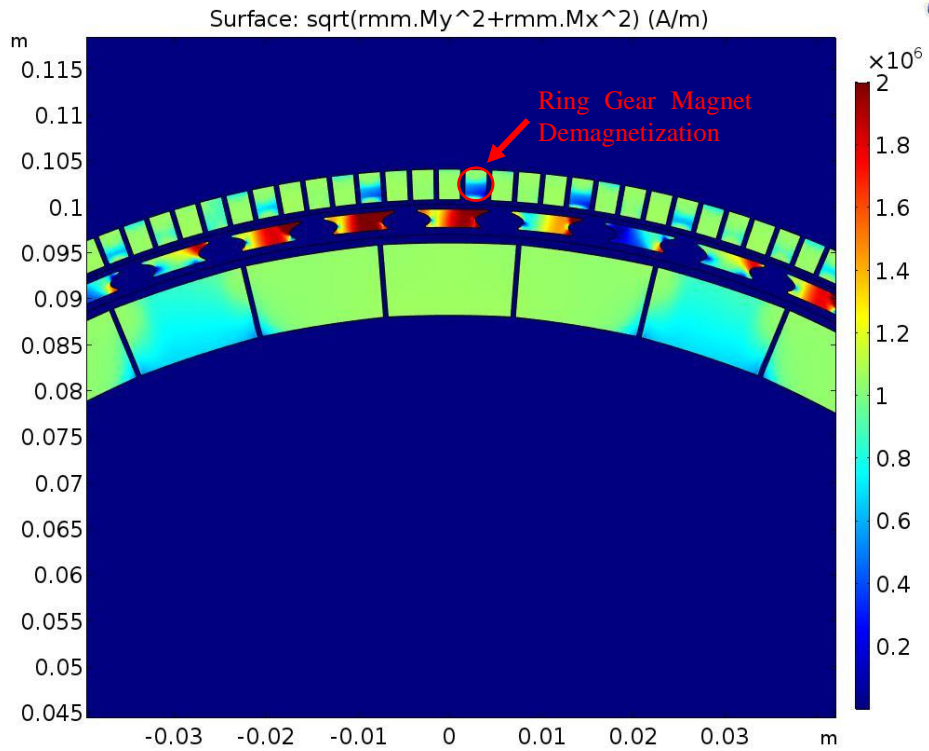

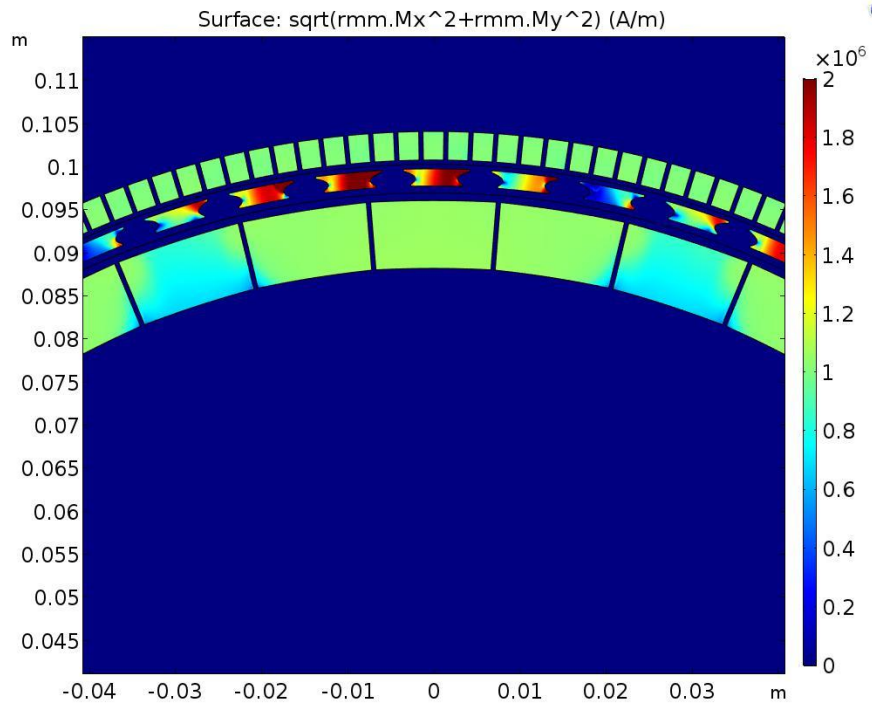**Figure 12 Demagnetization of tangentially oriented N52M ring gear magnets at 80℃**

Figure 13 Plot of magnetization with N48SH ring gear magnets and N52M sun gear magnets at 80℃ operating temperature. No significant demagnetization is observed in the ring gear magnets.

Table 2 Resulting torques from different magnet grade selection at 80℃

Sun Magnet Material	Ring Magnet Material	Torque at 80℃ (Nm)
N52M	N52M	278
N50H	N50H	304
N48SH	N48SH	303
N52M	N50H	300
N52M	N48SH	301
N50H	N48SH	311

Table 3 Electromagnetic design parameters for PT-4

PT-4 Electromagnetic Design Parameters	
Sun Pole Pairs	5
Modulator Pole Pieces	61
Ring Pole Pairs	56
Magnetic OD (mm)	104.1
Axial Length (mm)	52
Sun Magnet Thickness (mm)	7.878
Modulator Thickness (mm)	2
Ring Magnet Thickness (mm)	3.302
Inner Pole Piece Span Angle	4
Mid Pole Piece Span Angle	2.3
Outer Modulator Span Angle	5.44
Pole Piece Fillet Radius (mm)	0.127
Sun Magnet Mass (kg)	1.732
Ring Magnet Mass (kg)	0.687
Pole Piece Mass (kg)	0.287
Magnetic Mass (kg)	2.705
2D EM Specific Torque at 80C (Nm/kg)	108
2D EM Specific Torque at 20C (Nm/kg)	137

B. Electromagnetic Efficiency Analysis

In order to reduce computational cost and avoid having to do a simulation for each operating point of PT-4, PT-4's efficiency was modeled using a collection of 2D static FEA simulations and post processing equations rather than time-dependent FEA. Using this method, an approximation of the losses is made as the bidirectional coupling of the magnetic and electrical fields is neglected. For PT-4, 224 evenly spaced static simulations evaluated over one fifth of a sun gear rotation (the period of repetition for the sun gear) and the corresponding modulator rotation were used. Magnetic flux density data as a function of sun gear angular position was extracted from the simulations and post processed using the iron and magnet eddy current loss models described in the appendix.
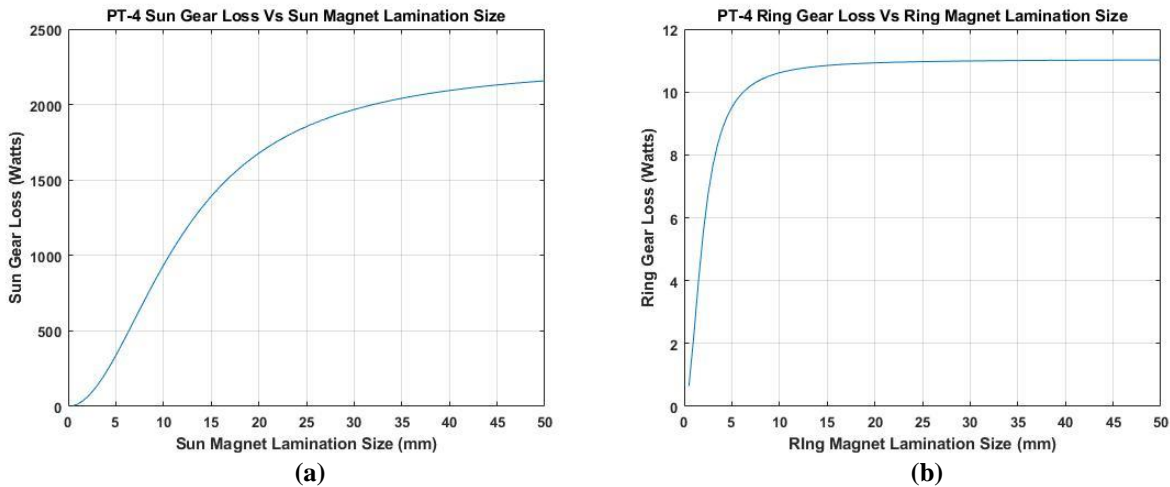
1. Magnet Lamination Size Selection

(a)   **(b)**

Figure 14 Effects of Sun and Ring Magnet Lamination Size on Sun and Ring Gear Magnetic Eddy Current Losses

The variation in sun gear and ring gear magnet eddy current loss with respect to sun and ring magnet lamination size is shown in Figure 14. Comparing sun gear losses in 14a to ring gear losses in 14b at similar magnet lamination sizes, the ring gear losses are an order of magnitude lower. This large difference in loss exists for three reasons.

The first reason is the width of the sun magnets (about 12 mm) is significantly larger than the width of the ring gear magnets (about 2 mm). In the absence of axial magnet laminations, the width is the smallest length scale in the magnets of the sun and ring gear and therefore the effective resistance of the magnets to eddy current generation is highly dependent on it. When the width of a magnet is much less than its length, the loss in that magnet scales with the width cubed. As a result, the effective resistance of the ring gear magnets is much higher than the resistance of the sun gear magnets when the lamination size is large. Magnet lamination size does not affect losses until it is close to the width of the magnet. Figure 14, shows this phenomenon as ring loss is essentially constant with lamination size until the laminations are about 10 mm in size.

The second reason sun gear loss is higher than ring gear loss is the larger volume of the sun gear magnets relative to the ring gear magnets. Eddy current loss scale linearly with magnet volume if the electrical potential generated is constant. The total volume of the sun gear magnets is 2.5 times the volume of the ring gear magnets.

The third reason is the relative frequencies of pole passage for each member. The frequency of ring gear pole passage on the sun is 11.2 times the frequency of the sun gear pole passage on the ring. Eddy currents in magnets scale with both the square of the frequency and the square of the magnitude of the time varying magnetic field. Because PT-4's modulator is only 2 mm in thick, unmodulated flux from both the sun and ring gear reaches the opposite magnet rotor. The magnitude of the unmodulated ring gear flux that reaches the sun is lower than the magnitude of the unmodulated sun gear flux that reaches the ring, however it is only lower by a factor of about 6. The ring gear, therefore, because of its 11.2 times higher frequency, produces more electrical potential on the sun gear in PT-4 as a result of its higher electrical frequency.

How the losses in Figure 14 translate to efficiency values is shown in Figure 15. As would be expected, efficiency does not appear to vary with ring magnet lamination size. For manufacturing simplicity, PT-4's ring gear magnets were therefore left unlamented. Sun magnet lamination size is shown to have a significant effect on efficiency in Figure 15. Based on manufacturing difficulties experienced with PT-3's magnets that had a 1 mm lamination thickness, a 2 mm lamination thickness was selected for PT-4 sun's magnets. This selection results in a predicated electromagnetic efficiency for the gear of 98.89%. If 1 mm or 1.5 mm laminations were used, efficiencies of greater than 99% would be achieved.
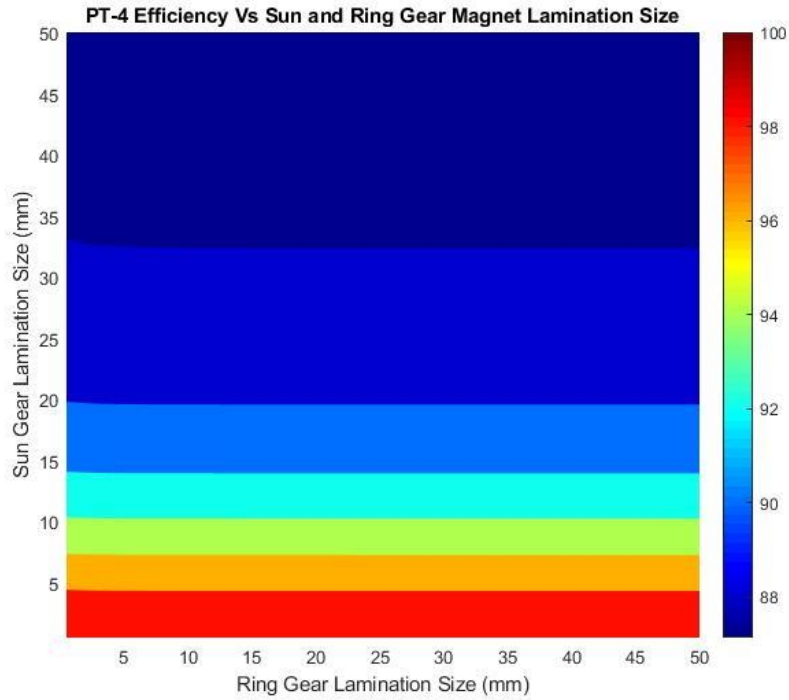
Figure 15 PT-4 efficiency vs magnet lamination size. Little dependence on ring gear magnet lamination size is shown.

2. Final Design Efficiency and Losses

An efficiency map for PT-4 at an operating temperature of 20℃ is shown in figure 16. The efficiency map shown in Figure 16 includes windage and bearing loss estimates calculated with analytical equations. The nominal operating point for the gear is marked with an X. The predicated efficiency at this operating point is ~98.5%. This efficiency exceeds the targeted 97% efficiency.
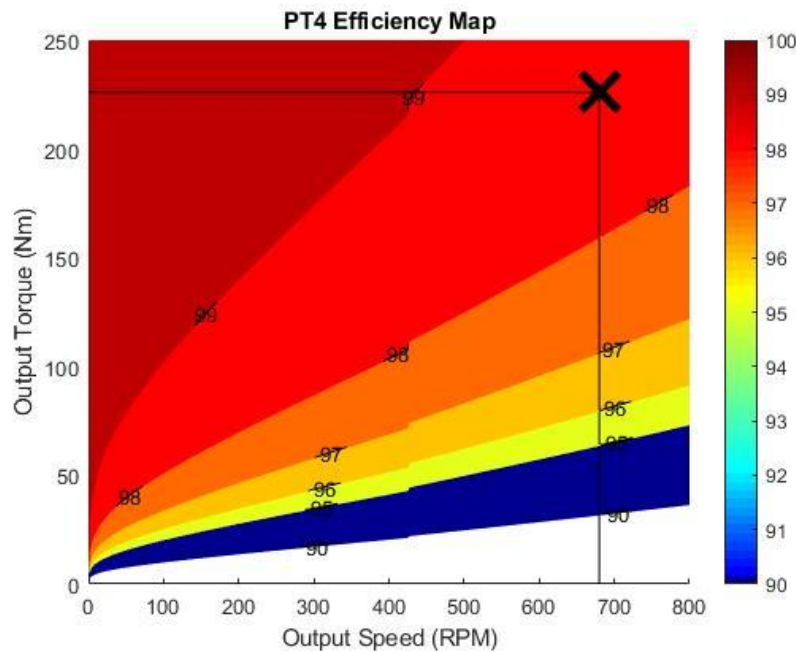

Figure 16 PT-4 Efficiency Map at 20℃ Operating Temperature

For magnetic gears, as operating temperature increases the efficiency of the gear increases as long as the gear can still achieve the desired torque at the operating speed. This increase in efficiency results from a decrease in the remanent flux density of magnets with increased temperature. The reduction in remanent flux in turn results in less time varying flux in the gear and therefore less magnetic loss. Additionally, NdFeB's resistivity increases with increase temperature and correspondingly leads to an additional drop in the magnitude of the eddy currents generated in the magnets. This drop-in magnet losses caused by the resistivity increase, is small compared to the loss reduction caused by the reduced remanent flux however. Figure 17 below shows a comparison of the magnetic losses at 20℃ and 80℃. Overall the drop-in losses with increase temperature results in an increase of efficiency to >99%. It should be noted that the drop-in magnet remanent flux density with temperature also reduces the max torque the gear can produce. The decrease in achievable 2D torque for PT-4 verses temperature is shown in Table 4.
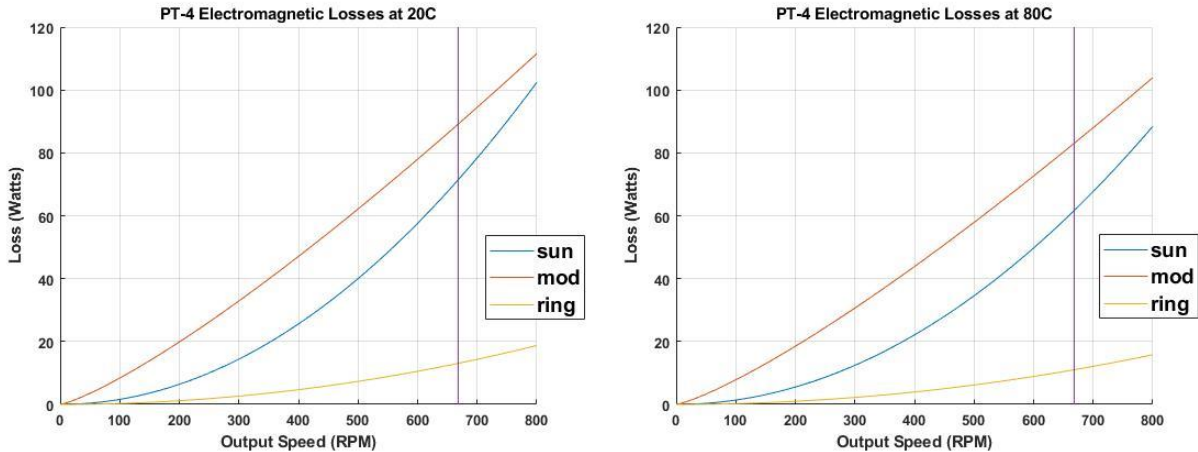

Figure 17 Comparison of PT-4 magnetic losses at 20℃ and 80℃

Table 4 PT-4 2D torque versus temperature

Temperature (°C)	Maximum 2D Output Torque (Nm)
20	370
80	303
100	270

VI.   Thermal Analysis

A centripetal pumping cooling flow scheme was selected for cooling PT-4. Conduction of heat from the modulator and sun gear magnets to the outer surface of a CMG is severely limited because of their rotational speed relative to the ring gear. Internal cooling flow is therefore required to cool the modulator and sun gear of a CMG. Centripetally pumped flow was selected because it makes use of the radial fluid flow produced by the high-speed rotation of the sun rotor and does not induce additional windage losses like axial flow through the gear's airgaps would.

A coupled fluid flow and thermal FEA model was built using a commercial FEA package to analyze this cooling approach. Symmetry was used across the gears' axial mid-plane and tangential arc to reduce model size. The geometry of PT-4 was de-featured and simplified to reduce computational cost. A conservative ambient temperature of 40℃ was assumed. A few iterations of the solidity of the modulator rotor cap geometry were completed to improve the radial flow through the axial gap between the sun rotor and modulator caps. Additionally, the pole piece support post carbon fiber selection was switched from IM7 fibers assumed in the code to a pitch-based carbon fiber with a thermal conductivity of >100 W/m*K. The resulting thermal results are depicted in Figure 18. Table 5 lists the max temperature of the three magnetic components. Both magnet arrays are kept below their assumed design operating temperature. The pole pieces have a slightly higher temperature due to the high concentration of losses in PT-4's pole pieces.
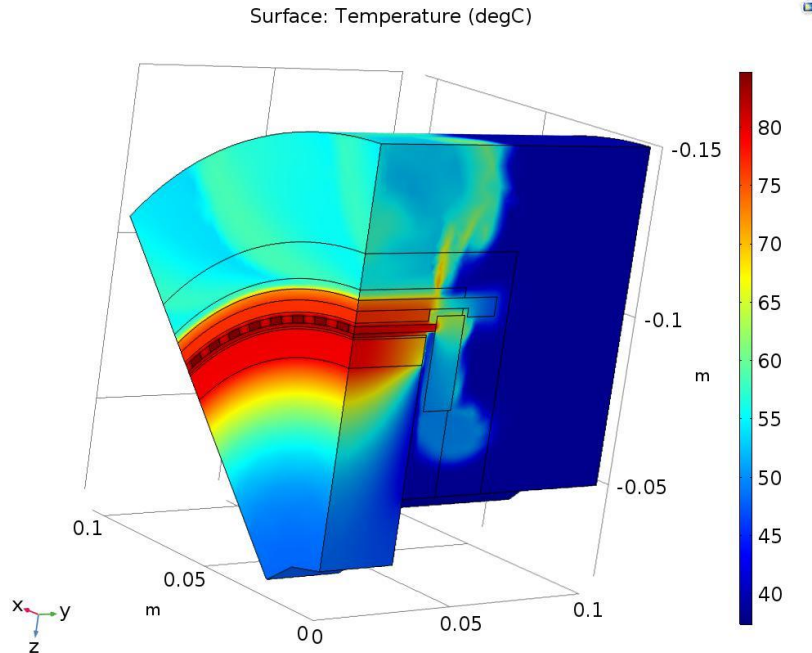
Figure 18 Temperature results for PT-4 thermal analysis

Table 5 Max Magnetic Component Temperatures from Thermal Analysis

Magnetic Component	Max Temperature
Sun Gear Magnets	80°C
Pole Pieces	85°C
Ring Magnets	77°C

VII.   Structural Design

The structural design of PT-4 is depicted in Figure 19. Most of the structure is composed of 3D printed carbon fiber reinforced nylon plastic. Retaining hoops and the modulator pole piece support posts are composed of unidirectional carbon fiber composite. The predicted mass for the design is 4.6 kg. This mass is only 8% higher than the mass predicted by the design code and 0.1 kg above the targeted mass for PT-4 (4.5 kg). The discrepancy between the design code predicted mass and the final mass mostly results from structural features that were added in the final design but not accounted for in the design code. For example, as can be seen in Figure 19, a number of shaft features (step changes, rotor connections) were required in the final mechanical design that were not accounted for in the design code's hollow shaft mass estimate. A margin factor needs to be added to the code going forward to account for these features. Additionally, the axial and radial loads from the bearings were not accounted for in the design code's estimation of the ring gear's mechanical support structure's mass. A more detailed analysis of the ring gear's structure needs to be built into the code.
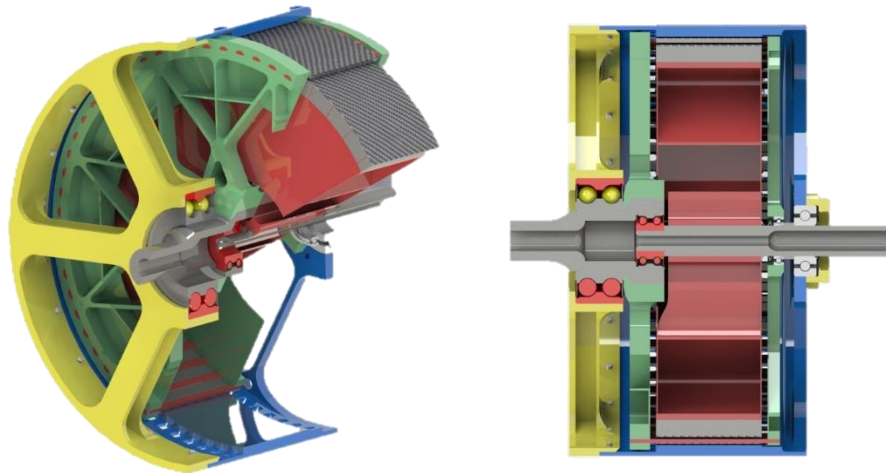
Figure 19 Final structural design of PT-4.

One other discrepancy between the design code's mechanical design and the final mechanical design is in the modulator's structure. As discussed in references 11-14, NASA has found modulator mass and thereby modulator radial thickness to be a main driver of a CMG's specific torque. The optimum modulator thickness, for electromagnetic specific torque, is often much thinner than is mechanically possible to achieve because of the large magnetic forces on the modulator. Figure 20 shows the variation in force on a single pole piece of PT-4 during one period of repetition. To account for these large loads, the design code assumed that PT-4's modulator posts where unidirectional IM-7 carbon fiber, and the calculation of the stresses in the posts were included as a key part of the design code. However, the initial structural FEA of PT-4's modulator indicated that the deflection in those posts was greater than 0.5 mm (over half of the unloaded airgap) despite a peak stress of around 350 MPa (only 44% of the stress-based design limit). As a result, alternative structural options were explored during the detailed design phase with the goal of maximizing the remaining physical gap between the ring gear and the modulator when the modulator is fully loaded.
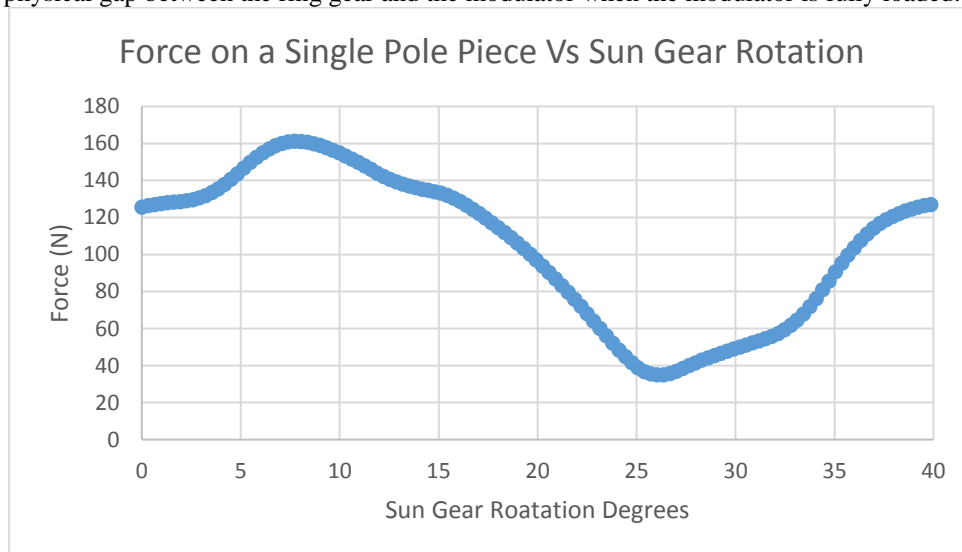

Figure 20 Electromagnetic force on a single modulator pole piece vs sun gear rotation

The final solution selected, shown in Figure 19, uses a carbon fiber hoop on the outer diameter of the modulator and stiffer pitch-based carbon fiber in the pole pieces. This solution enables a remaining ring-modulator airgap of 0.67 mm under full load. Overall, the results of this analysis point to the need to account for both stresses and deflections of the modulator support posts in future revisions of the design code

VIII.   Conclusion

In this paper, the design of a magnetic gear (PT-4) for NASA's RVLT project's vertical lift quadrotor reference vehicle was presented. PT-4 is designed to be a demonstrator of a high specific torque and high efficiency magnetic gear for electrified aircraft. It is also NASA's step towards a higher technology readiness demonstrator for an electrified aircraft magnetic gearbox as all the propeller and flight loads for the quadrotor reference vehicle are accounted for in its design. The preliminary design of this gear was created with the use of a new magnetic gear design code that combines structural and electromagnetic analyses. With the guidance of the design code, the completed final design achieves a predicted mass of 4.6 kg (49 Nm/kg) and a predicted efficiency of 98.5% at the nominal operating condition. The high efficiency of PT-4 is enabled by the use of Halbach arrays and sun gear magnet laminations. A centripetal pumped cooling flow scheme was implemented for self-cooling. Even with the additional design constraints for PT-4 compared to PT-2, PT-4 is expected to exceed the specific torque record set by PT-2 and set the new state of the art for the achievable specific torque in a CMG.

The newly developed design code enables selection of a preliminary design in less than a week. The mass of the preliminary design was heavier than the final design mass by only 8%. This 8% difference resulted from multiple reasons as was discovered during the detailed design phase of this project. Recommendations for improving the preliminary design produced by the code include the following:
1. In the design of a magnetic gear with Halbach array magnet rotors, minimum ring magnet width as well as minimum magnet thickness needs to be set to avoid significant demagnetization,
2. At a given temperature the highest magnet grade that can operate at that temperature does not necessarily produce a magnetic gear with the highest specific torque,
3. The modulator support structure's stiffness becomes equally as important as its strength when the modulator's thickness is minimized to minimize mass,
4. Assuming straight shafts and not accounting for their complex attachment features can lead to an underestimate of the shafts' mass
5. The ring gear's structure needs to be analyzed more thoroughly in the design code, because of the significant loading the propeller imparts on it.

IX.   Appendix

A. Magnet Eddy Current Model
Eddy currents in the magnets were predicted using the eddy current model for general periodic waves found in Ref 21. The model defines volumetric loss in a component experiencing a periodically varying magnetic field as

$$P_c = \frac{1}{16} \frac{V}{\rho} \frac{w^2 l^2}{w^2 + l^2} \frac{1}{T} \int_0^T (\frac{dB}{dt})^2 \, dt$$

Where P_c is the volumetric loss, w the tangential thickness of the magnet, l is the axial length of a magnet segment or lamination, V is the volume of the magnet, ρ is the resistivity of the material, T is the period of repetition, and B is magnetic field magnitude.
Using numeric integration, the above equation can be written as

$$P_c = \frac{1}{16} \frac{V}{\rho} \frac{w^2 l^2}{w^2 + l^2} \frac{1}{\Delta t * N} \sum_{i=1}^{N} (\frac{\Delta B_i}{\Delta t_i})^2 \, \Delta t_i$$

Where N is the number of time steps and Δt is the length of the time step. Because Δt is constant this equation can be simplified to

$$P_c = \frac{1}{\Delta t^2} \frac{1}{16} \frac{V}{\rho} \frac{w^2 l^2}{w^2 + l^2} \frac{1}{N} \sum_{i=1}^{N} \Delta B_i^2$$

B. Pole Piece Iron Loss Model
Modulator loss was predicted using the Improved Generalized Stienmetz Equation (IGSE) with minor loop separation method found in reference 22. The IGSE is a modification to the Stienmetz Equation that allows for accurate prediction of core loss when the magnetic field is not sinusoidal. The Stienmetz Equation defines the specific core loss (loss per Kg of material) in electrical steel subjected to a sinusoidal varying magnetic field as

$$P_v = k * f^\alpha B^\beta$$

Where P_v is specific core loss, f is the frequency of the sinusoidal varying magnetic field, B is the peak value of the field, and k, α, and β are material constants. k, α, and β can generally be determined from core loss information provided by electrical steel manufacturers. The IGSE uses these parameters to predict core loss for non-sinusoidal waves as

$$P_v = \frac{1}{T}\int_0^T k_1 \left|\frac{dB}{dt}\right|^\alpha (\Delta B)^{\beta-\alpha} dt$$

$$k_1 = \frac{k}{2^{\beta-1}\pi^{\alpha-1}\int_0^{2\pi}|\cos(\theta)|^\alpha d\theta}$$

Where T is the period of repetition of the field, ΔB is the peak to peak flux density, and k_1 is an updated loss coefficient. The algorithm for numerically implementing this equation with minor loop separation is discussed in detail in reference 20. This algorithm was implemented on the magnetic flux density versus rotor position data from the simulation. By a similar method as used for the magnet loss, modulator loss can also be written

$$Loss_{mod} = C_{mod} * \left(\frac{1}{\Delta t}\right)^\alpha$$

Where $Loss_{mod}$ is the modulator losses and C_{mod} is the modulator loss coefficient.

This loss prediction is only meant to serve as a minimum baseline for modulator loss in the gear as the IGSE most likely under predicts the losses. The IGSE is only accurate for unidirectional fields and therefore it doesn't account for the losses from the rotating fields (Ref 23). Therefore, iron loss is most likely under predicted.

X.   Acknowledgments

XI.   References

1.   Anderson, A.D., Renner, N.J., Wang, Y., Lee, D., Agrawal, S., Sirimanna, S., Haran, K., Banerjee, A., Starr, M., and Felder, J., "System Weight Comparison of Electric Machine Topologies for Electric Aircraft Propulsion" 2018 AIAA/IEEE Electric Aircraft Technologies Symposium. Cincinnati, Ohio.

2.   Astridge, D., and Savage, M., "Rotorcraft Drivetrain Life Safety and Reliability," AGARD Report No. 775, North Atlantic Treaty Organization Advisory Group For Aerospace Research And Development, June 1990

3.   Zaretsky, E. V., "Bearing and Gear Steels for Aerospace Applications" NASA Technical Memorandum 102529, NASA, March 1990

4.   Desvaux, M., Bildstein, H., Sire, S., and Fasquelle, A., "Magnetic Losses and Thermal Analysis in a Magnetic Gear for Wind Turbine," 13th International Conference on Ecological Vehicles and Renewable Energies, IEEE, 2018

5.   Johnson, M., Gardner, M.C., Toliyat, H. A., Englebretson, S., Ouyan, W., and Tschida, C., "Design, Construction, and Analysis of a Large-Scale Inner Stator Radial Flux Magnetically Geared Generator for Wave Energy Conversion," IEEE Transactions on Industrial Applications Vol 50 No 4, July/August 2018

6.   McGilton, B., Crozier, R., McDonal, A., and Mueller, M., "Review of Magnetic Gear Technologies and Their Applications in Marine Energy," IET Renewable Power Generation Conference, IET, December 2017

7.   Frandsen, T.v., Rasmussen P.O., and Jensen K.K., "Improved Motor Integrated Permanent Magnet Gear for Traction Applications," 2012 IEEE Energy Conversion Congress and Exposition (ECCE)

8.   Jian, L., Chau, K.T., and Jian, J.Z., " An Integrated Magnetic-Geared Permanent-Magnet In-Wheel Motor Drive for Electric Vehicles," IEEE Vehicle Power and Propulsion Conference, IEE, September 3-5, 2008

9.   Jansen, R., Brown, G. V., Felder, J. L., and Duffy, K. P., "Turboelectric Aircraft Drive Key Performance Parameters and Functional Requirements," American Institute of Aeronautics and Astronautics, 2015

10. Kirsten P. Duffy and Ralph Jansen. "Partially Turboelectric and Hybrid Electric Aircraft Drive Key Performance Parameters", 2018 AIAA/IEEE Electric Aircraft Technologies Symposium, AIAA Propulsion and Energy Forum, (AIAA 2018-5023)

11. Asnani, V., Scheidler, J., and Tallerico, T., "Magnetic gearing research at NASA," Proc. of AHS Int. 74th Annual Forum, Phoenix, AZ, May 14-17, 2018.

12. Scheidler, J. J., Asnani, V. M., and Tallerico, T. F., "NASA's magnetic gearing research for electrified aircraft propulsion," Proc. of AIAA/IEEE Electric Aircraft Technologies Symposium, Cincinnati, OH, Aug 21-22, 2018.

13. Scheidler, J.J., Cameron, Z. A., and Tallerico, T. F., "Dynamic Testing of a High Specific Torque Concentric Magnetic Gear," Proc. of the Vertical Flight Society's 75th Annual Forum, Philadelphia, PA, May 13-16, 2019

14. Cameron, Z. A., Tallerico, T. F, and Scheidler, J.J. "Lessons Learned in Fabrication of a High-Specific-Torque Magnetic Gear," Proc. of the Vertical Flight Society's 75th Annual Forum, Philadelphia, PA, May 13-16, 2019

15. Johnson, W., Silva, C., and Solis, E., "Concept Vehicles for VTOL Air Taxi Operations," American Helicopter Society Technical Conference on Aeromechanics Design for Transformative Vertical Flight, San Francisco, CA, Jan 16 – 19, 2018.

16. Atallah, K., Calverley, S., and Howe, D., "Design, analysis and realization of a high-performance magnetic gear," Proc. of IEEE Electric Power Applications, p. 135-143, 2004.

17. SKF Group, "SKF Rolling Bearings Catalogue," August, 2016. http://www.skf.com/binary/77-121486/SKF-rolling-bearings-catalogue.pdf,

18. Gerber, S. and Wang, R-J., "Analysis of the end-effects in magnetic gears and magnetically geared machines," 2014 International Conference on Electrical Machines Proceedings, Berlin, German, pp. 396 – 402, Nov. 2014.

19. Zhu, Z.Q., and Howe, D.: 'Influence of design parameters on cogging torque in permanent magnet machines', IEEE Trans. Magn., 2000, 15, (5), pp. 407–412

20. Jungmayr, G., Loeffler, J., Winter, B., Jeske, F., and Amrhein, W., "Magnetic gear: radial force, cogging torque, skewing, and optimization," IEEE Transactions on Industry Applications, p. 3822-3830, 2016.

21. Rouho, S., Santa-Nokki, T., Kolehmainen, J., and Arkkio, A., "Modeling Magnet Length in 2-D Finite Element Analysis of Electric Machine," IEEE Transactions on Magnetic Vol 45 No 8, IEEE, August 2009

22. K. Venkatachalam, C. Sullivan, T. Abdallah, and H. Tacca, "Accurate prediction of ferrite core loss with non-sinusoidal waveforms using only Steinmetz parameters," in Computers in Power Electronics, 2002. Proceedings. 2002 IEEE Workshop on, June 2002, pp. 36 – 41

23. A. Krings, "Iron Losses in electrical Machines – Influence of Material Properties, Manufacturing Processes, and Inverter Operation" Doctoral Thesis KTH University. Stockholm, Sweden 2014